Supplementary Information (SI) for Journal of Materials Chemistry A.
This journal is © The Royal Society of Chemistry 2025

Supporting information

Thiol-Modified Solid Electrolyte Interphase Enhances the Stability of Zinc Anodes under High Depth of Discharge

Jie Liu,[a] Peng Wang,*[a,b,c] Xiaoyu Yang,[a] Zinan Wang,[a] Hangyu Miao,[a] Zhe Li,[a] Wei Duan,[a,b] Ying Yue,[a,b] Yunpeng Liu [d] & Yang Ju [e]

[a] School of Energy, Power and Mechanical Engineering, North China Electric Power University, Baoding, 071000, China

[b] Hebei Key Laboratory of Electric Machinery Health Maintenance & Failure Prevention, North China Electric Power University, Baoding, 071003, China

[c] Key Laboratory of Icing and Anti/De-icing, China Aerodynamics Research and Development Center, Mianyang, Sichuan, 621000, China

[d] Department of Electrical Engineering, North China Electric Power University, Baoding, 071000, China

[e] School of Mechanical Engineering, Zhejiang University, Hangzhou, 310058, China

* Corresponding Author

E-mail: wangpeng1986@ncepu.edu.cn

Experimental section

Materials

Zinc foil (99.99%) and copper foil (99.99%) were purchased from Anhui Zhengying Metal Materials Co., Ltd. Titanium foil (99.99%) was purchased from Cyber Electrochemical Materials Co., Ltd. All experimental reagents used were of analytical grade and did not require further purification. Zinc trifluoromethanesulfonate ($Zn(OTF)_2$, AR, 98%), Tris[2-(3-mercaptopropionyloxy)ethyl] isocyanurate (TMPEI, AR, 98%) and Ethylene glycol (EG, AR, 98%) were purchased from Shanghai Macklin Biochemical Co., Ltd. Vanadium pentoxide (V_2O_5, AR, 99%) and Aluminum chloride hexahydrate ($AlCl_3\cdot6H_2O$, AR, 97%) were purchased from Aladdin Industrial Corporation. Ketjen Black and LA_{133} were purchased from Guangdong Zhuoguang New Energy Technology Co., Ltd. N-Methyl-2-pyrrolidone (NMP, AR) was purchased from Tianjin Kermel Chemical Reagent Co., Ltd. Hydrogen peroxide (H_2O_2, 30%) was purchased from Sinopharm Chemical Reagent Co., Ltd.

Preparation of the AlVO-NMP cathode

Typically, 0.364 g commercial V_2O_5 and 2 mL H_2O_2 (30%) were added into 60 mL deionized water under stirring. When V_2O_5 was dissolved, 2.414 g $AlCl_3\cdot6H_2O$ was added into the solution. After stirring for 0.5 h, the solution was transferred to a Teflon lined stainless steel autoclave and heated at 120 °C for 5 h, and then cooled to room temperature naturally. The precipitate was collected by filtration and then washing with deionized water. After drying the collected precipitate for 10 h at 60 °C in an electric oven, the product was obtained. The obtained product was mixed with Ketjen Black and LA_{133} in a weight ratio of 7:2:1. Subsequently, NMP was added, and the mixture was stirred evenly. Finally, the slurry was cast onto a titanium box to prepare the AlVO-NMP electrode. After drying at 80 °C for 10 h, an electrode with a mass loading of 0.5 mg cm^{-2} was obtained.

Battery assembly

For CR2032 coin cells, the Zn||Zn symmetric batteries used zinc foil (100 μm or 30 μm) as both the cathode and anode; the Zn||Cu half-cells used zinc foil (100 μm) as the anode and copper foil (100 μm) as the cathode; and the Zn||AlVO-NMP full cells utilized zinc foil (100 μm) or TMPEI-3@Zn (100 μm) as the anode, AlVO-NMP as the cathode, and 1 M $Zn(OTF)_2$ or 1 M $Zn(OTF)_2$ mixed with 0.02wt% TMPEI as the electrolyte (125 μL per cell). A single layer of GF/D (Whatman) glass fiber membrane (0.67mm) was used as the separator. The assembly method for pouch cells was identical to that of coin cells. For pouch cell, the cathode (AlVO-NMP) had dimensions of 40 mm × 40 mm, containing approximately 8 mg of active material (V_2O_5), while the anode (Zn foil) had dimensions of 50 mm × 50 mm.

Material characterizations

Water contact angles were measured at 25 °C using a custom-made contact angle meter. The experiments mentioned above were conducted with 5 μL water droplets.The surface morphology and structure were examined using a scanning electron (TESCAN Vega3) microscope and an optical profiler (Bruker Contour GT-K 3D).X-ray diffraction (XRD) patterns were obtained at a scanning rate of $2°\mathrm{min}^{-1}$ using Rigaku SmartLab SE (Cu Kαradiation).The chemical composition of the prepared electrode surface was evaluated using XPS (Thermo ESCALAB 250XI, USA).In situ observation of dendrites was performed using an optical microscope (CX-HV4800) and an in situ battery from Suzhou Vision Precision Instrument Co., Ltd.Fourier Transform Infrared (FTIR) spectra were collected on Thermo Scientific Nicolet iS20. The information regarding the crystal structure and the composition of the material was obtained using 1H nuclear magnetic resonance (NMR, using the BRUKER-AVANCE III HD 500 MHz spectrometer). Raman spectroscopy was obtained by Renishaw-inVia-Reflex using a 532 nm diode-pumped solid-state laser.

Electrochemical measurements

Under room temperature conditions, the electrochemical performance of half-cells and full-cells was investigated using CR2032 coin cells and pouch cells. The electrochemical analyses, including linear sweep voltammetry (LSV), Tafel plots, chronoamperometry (CA), cyclic voltammetry (CV), and electrochemical impedance spectroscopy (EIS), were conducted on a CHI 760E electrochemical workstation (Shanghai Chenhua). In the LSV measurements, hydrogen evolution reaction (HER) polarization curves were obtained at a scan rate of 5 mV s^{-1}. Tafel plots for the three-electrode configuration were obtained through linear fitting to determine the corrosion current density and corrosion potential. Chronoamperometry (CA) curves were recorded at an overpotential of 10 mV, and the resistance of the electrodes was measured before and after the tests. Ionic conductivity was measured in the frequency range of $0.01–10^5$ Hz. CV curves were tested at a scan rate of 0.1 mV s^{-1}. EIS was conducted over a frequency range of 100 mHz to 100 kHz. Galvanostatic charge-discharge tests were performed using the Neware battery testing system (BTS4000, Shenzhen, China).

The activation energy was calculated from the Arrhenius equation:

$$\frac{1}{R_{ct}} = Aexp\left(\frac{-E_a}{RT}\right) \tag{1}$$

where R_{ct}, A, R, and Trepresent charge transfer resistance, frequency factor, gas constant, and absolute temperature, respectively.

Zn^{2+} transfer numbers (tZn^{2+}) in the symmetric Zn cells were calculated by the Bruce-Vincent formula:

$$t_{Zn^{2+}} = \frac{I_S(\Delta V - I_0R_0)}{I_0(\Delta V - I_SR_S)} \tag{2}$$

In this context, ΔV represents the applied voltage polarization, I_S and R_S denote the steady-state current and resistance, and I_0 and R_0 represent the initial current and resistance. The applied polarization voltage here is 10 mV.

The surface energy of the zinc anode was calculated using the Owens-Wendt equation, which is as follows:

$$\gamma_L(1 + cos\,\theta) = 2\left(\sqrt{\gamma_S^d * \gamma_L^d} + \sqrt{\gamma_S^p * \gamma_L^p}\right) \tag{3}$$

In this context, γ_L represents the total surface tension of the liquid, while γ_L^d and γ_L^p denote the dispersive and polar components of the liquid's surface tension, respectively.

The calculation of the total surface energy is as follows:

$$\gamma_S = \gamma_S^d + \gamma_S^p \tag{4}$$

In this context, γ_S represents the total surface energy, while γ_S^d and γ_S^p denote the dispersive and polar components of the surface energy, respectively.

Density Functional Theory (DFT) calculations

DFT calculations were conducted using the Gaussian software. Geometry optimizations and single-point energy calculations were performed employing the B_3LYP functional combined with the 6-31G(d, p) basis set.

The binding energy of E_{bind} was defined as the following equation:

$$E_{bind} = E_{tot} - (E_{part\,1} + E_{part\,2}) \tag{5}$$

where E_{tot}, $E_{\mathrm{part\ 1}}$ and $E_{\mathrm{part\ 2}}$ refer to the total energies of system, TMPEI, and H_2O/Zn^{2+}, respectively.

The adsorption energy of E_{ads} was defined as the following equation:

$$E_{ads} = E_{tot} - (E_{part\,1} + E_{part\,2}) \tag{6}$$

where E_{tot}, $E_{\text{part 1}}$ and $E_{\text{part 2}}$ refer to the total energies of system, Zn slab, and TMPEI/H_2O, respectively.

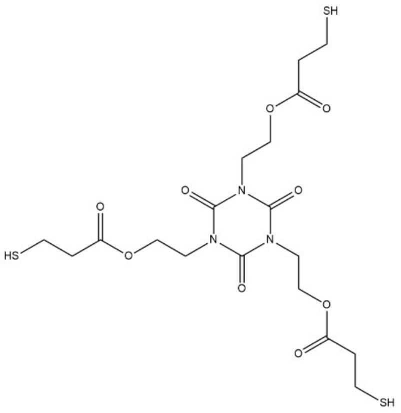

Fig. S1 Chemical structure of Tris[2-(3-mercaptopropionyloxy)ethyl] isocyanurate (TMPEI).

The molecular structure of TMPEI is centered around a six-membered ring constructed by an isocyanurate group (-N=C-NH-), with three branched chains attached via ester linkages (-$COOCH_2CH_2$-) to terminal thiol groups. The isocyanurate group exhibits significant chemical stability, typically resisting oxidation or reduction reactions in electrolytes or electrochemical processes. The ester group demonstrates good stability in neutral or mildly acidic environments, especially under low potential conditions, where hydrolysis is unlikely to occur. The stability of both the isocyanurate and ester groups ensures the structural integrity of the TMPEI molecule during prolonged cycling.

Additionally, in the TMPEI molecule, the alkyl portion of the ester group (-CH_2CH_2-) is a nonpolar moiety, typically exhibiting hydrophobic properties. This alkyl chain segment is less likely to form hydrogen bonds with water molecules, thus it tends to avoid aqueous environments, contributing to its hydrophobic nature. Although the thiol group itself is polar, its interaction with water is relatively weak, especially when hydrophobic segments are present in the molecule, resulting in an overall enhanced hydrophobicity.

Based on the molecular structure, it can be inferred that the TMPEI molecule possesses a stable core structure and likely interacts with the external environment primarily through its terminal thiol group. The thiol group exhibits strong gold affinity and some hydrophobicity, which facilitates its stable adsorption on the zinc anode surface while suppressing side reactions such as HER. Traditional zinc anode coatings and SEI layers may detach over prolonged cycling. However, due to the stable core structure and excellent gold affinity of TMPEI, it is likely to re-adsorb onto the zinc anode surface even after detachment, thereby providing more efficient protection.

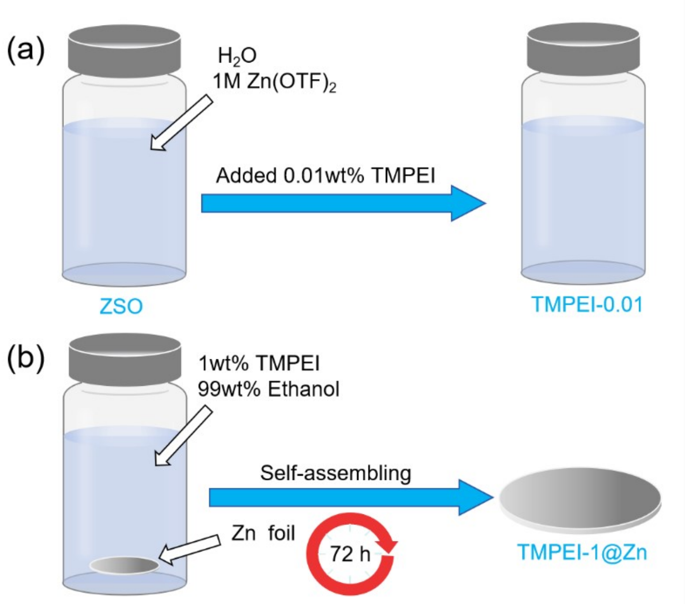

Fig. S2 (a) Preparation of TMPEI-0.01 modified electrolyte and (b) Preparation of TMPEI-1@Zn modified electrode.

The ZSO electrolyte was prepared by dissolving 1 M zinc trifluoromethanesulfonate ($Zn(OTF)_2$) in water. Next, 0.01 wt% TMPEI was added to the ZSO solution to create the TMPEI-0.01 modified electrolyte. The TMPEI-1@Zn modified electrode was then prepared by soaking zinc foil in an ethanol solution containing 1 wt% TMPEI for 72 h. By adjusting the TMPEI mass fraction, different combinations of TMPEI-n modified electrolytes and TMPEI-n@Zn modified electrodes were prepared.

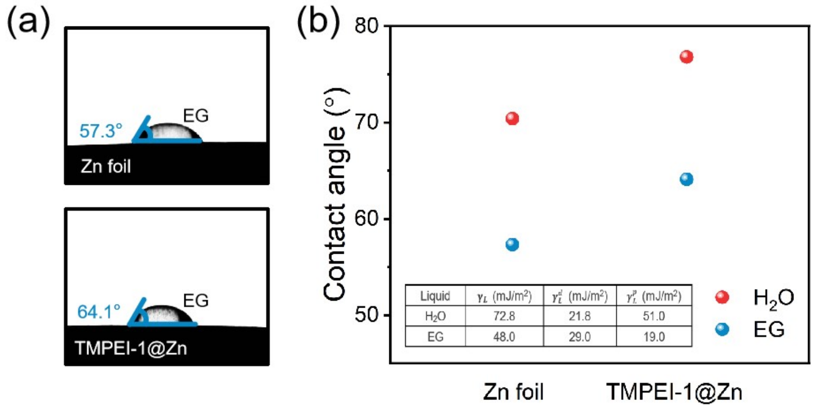

Liquid	γ_L (mJ/m²)	γ_L^d (mJ/m²)	γ_L^p (mJ/m²)
H_2O	72.8	21.8	51.0
EG	48.0	29.0	19.0

Fig. S3 (a) EG contact angles of zinc foil and TMPEI-1@Zn modified electrode and (b) Contact angle data of EG and H_2O on zinc foil and TMPEI-1@Zn modified electrode (insets show the known parameters of H_2O and EG).

To further investigate the modification effect of TMPEI on the hydrophobicity of the zinc anode surface, ethylene glycol (EG) contact angle measurements were conducted in addition to the water contact angle measurements (Fig. 1d), as shown in Fig. S3. Subsequently, surface energy calculations for the modified and unmodified zinc anodes were performed using the Owens-Wendt equation based on the aforementioned data. Detailed calculation methods can be found in the experimental section. The results, presented in Table S1, show that the total surface energy (γ_S) of Zn foil is 40.3 mJ/m², while that of TMPEI-1@Zn is 33.2 mJ/m². These findings indicate a 17.6% reduction in γ_S after TMPEI modification, suggesting an enhancement in the hydrophobicity of the zinc anode, which is consistent with the water contact angle measurements.

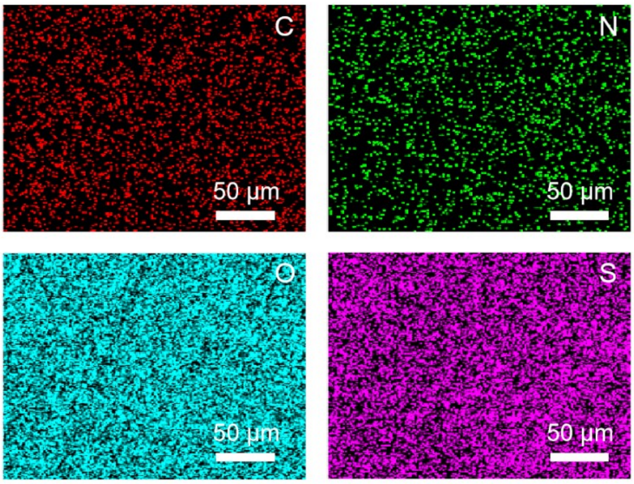

Fig. S4 EDS mapping of carbon, nitrogen, oxygen, and sulfur element distribution on the zinc anode of the TMPEI-0.01 cell after 100 h of galvanostatic cycling at 1 mA cm^{-2} and 1 mAh cm^{-2}.

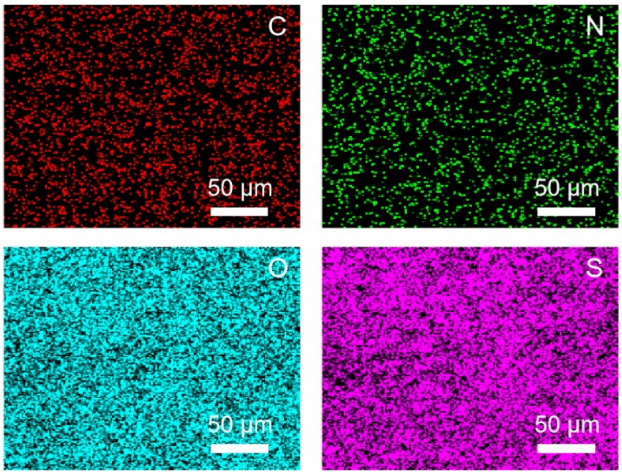

Fig. S5 EDS mapping of carbon, nitrogen, oxygen, and sulfur element distribution on the zinc anode of the ZSO+TMPEI-1@Zn cell after 100 h of galvanostatic cycling at 1 mA cm⁻² and 1 mAh cm⁻².

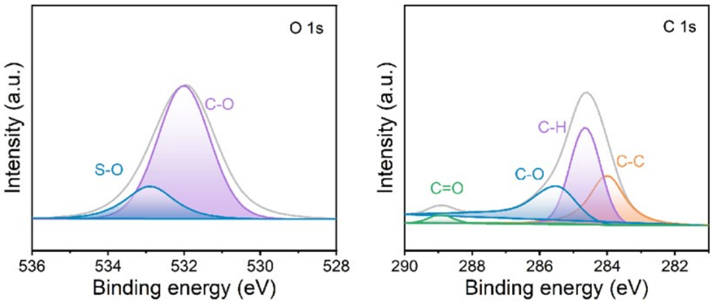

Fig. S6 O 1s and C 1s spectra of the zinc anode in the TMPEI-0.01 cell.

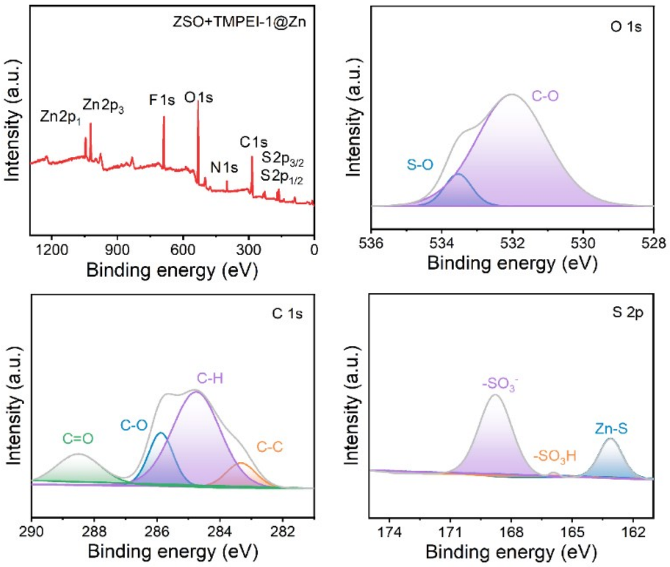

Fig. S7 XPS spectra of the zinc anode in the ZSO+TMPEI-1@Zn cell, along with the corresponding high-resolution O 1s, C 1s, and S 2p spectra.

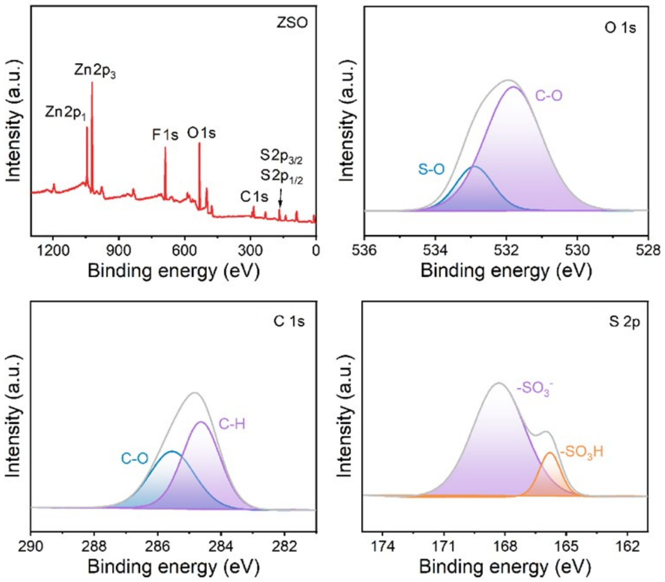

Fig. S8 XPS spectra of the zinc anode in the ZSO cell, along with the corresponding high-resolution O 1s, C 1s, and S 2p spectra.

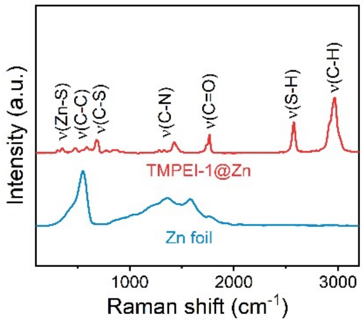

Fig. S9 Raman spectra of the surfaces of unmodified zinc foil and TMPEI-1@Zn modified electrode.

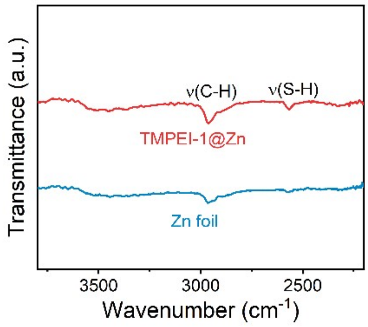

Fig. S10 FTIR spectra of the surfaces of unmodified zinc foil and TMPEI-1@Zn modified electrode.

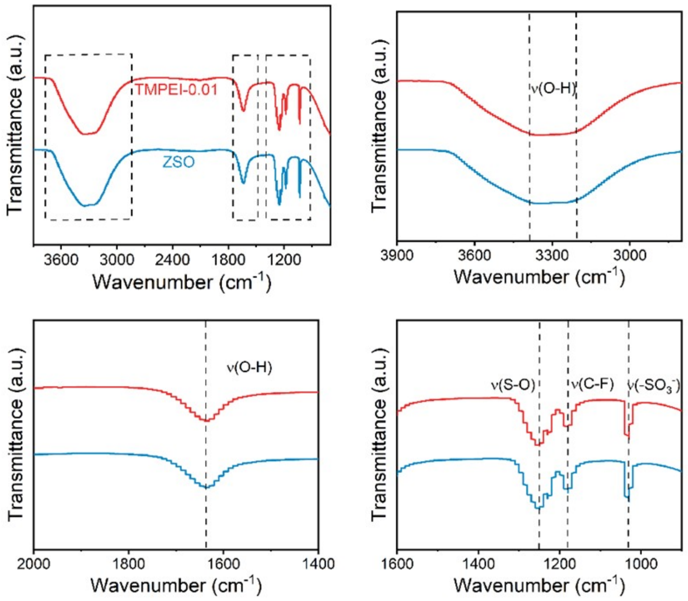

Fig. S11 FTIR spectra of TMPEI-0.01 and ZSO electrolytes.

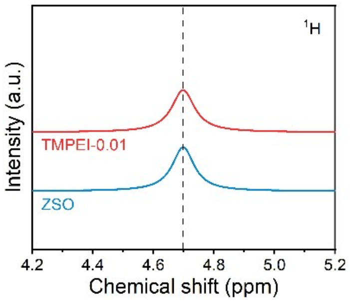

Fig. S12 NMR spectra of TMPEI-0.01 and ZSO electrolytes.

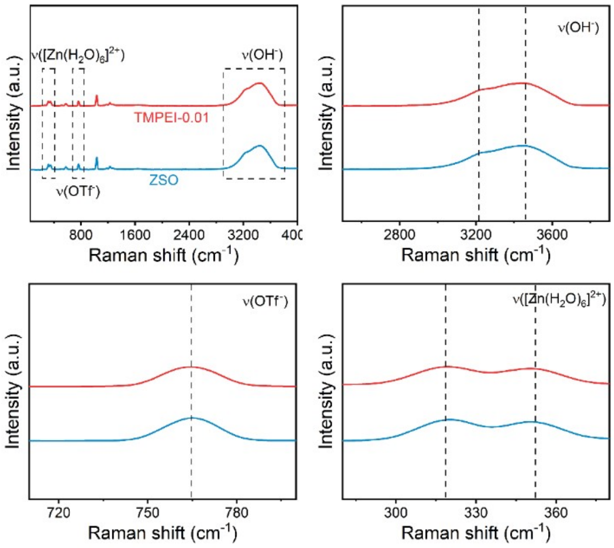

Fig. S13 Raman spectra of TMPEI-0.01 and ZSO electrolytes.

To investigate whether TMPEI affects the solvation structure of zinc ions and the water activity in the solution, FTIR, NMR, and Raman spectroscopy were utilized. The FTIR results

(Fig. S11) indicate that the stretching vibration (3000–3800 cm^{-1}) and bending vibration (1600–1700 cm^{-1}) of the hydroxyl group showed no significant changes, suggesting that TMPEI does not influence the vibration modes of these groups. Similarly, nuclear magnetic resonance analysis (Fig. S12) revealed no substantial alterations in the characteristic peaks of the 1H NMR spectrum, implying that TMPEI does not affect the chemical environment of the hydrogen atoms in the electrolyte. In the Raman spectrum (Fig. S13), the characteristic vibrational peaks of $[Zn(H_2O)_6]^{2+}$ (300–400 cm^{-1}), OTf^{-} (750–780 cm^{-1}), and OH^{-} (3000–3700 cm^{-1}) remained unchanged following the introduction of TMPEI. The consistency of results from these three techniques provides strong evidence that TMPEI does not modify the solvation structure of Zn^{2+} ions or the water activity in the solution.

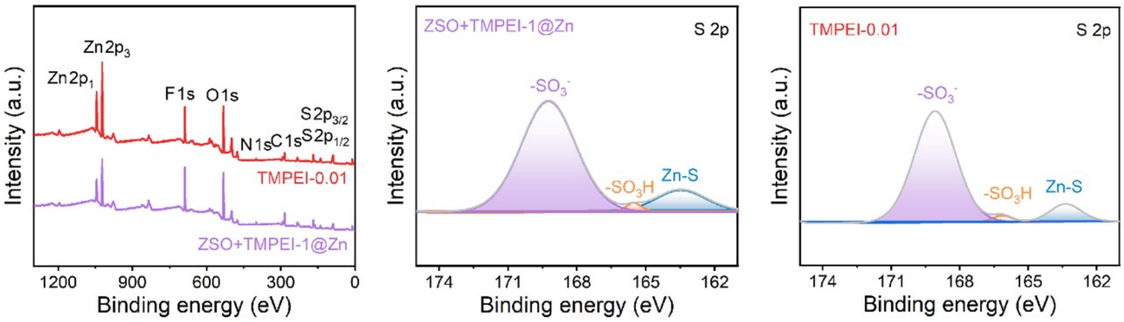

Fig. S14 XPS spectra of the ZSO+TMPEI-1@Zn and TMPEI-0.01 cells after 100 h of galvanostatic cycling at 5 mA cm^{-2} and 20 mAh cm^{-2}, along with the corresponding high-resolution S 2p spectra.

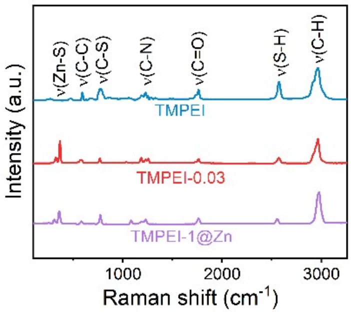

Fig. S15 The Raman spectra of TMPEI-0.03 zinc anode, TMPEI-1@Zn zinc anode, and TMPEI molecules.

We investigated the long-term stability of TMPEI SEI layer and its potential degradation effects, as well as whether TMPEI might undergo unnecessary chemical reactions with electrolyte components during long-term cycling (Fig. S15). Specifically, Raman tests were performed on the zinc anodes of TMPEI-0.03 batteries (Fig. 4a) and TMPEI-1@Zn batteries

(Fig. S27) after cycling, and additional tests were conducted on the TMPEI material. The results show that the chemical bond fluctuations on the surfaces of both battery zinc anodes are similar to those of the TMPEI material, with the addition of Zn-S bond fluctuations. This indicates that after long-term cycling, TMPEI remains stably adsorbed on the zinc anode, with its structure intact and without degradation. Moreover, the absence of new chemical bond fluctuations suggests that TMPEI does not undergo side reactions with other electrolyte components during long-term cycling. Furthermore, combining FTIR, NMR, and Raman (Fig. S11-13) results of the electrolyte, we can infer that the introduction of TMPEI does not trigger any potential side reactions or unexpected interactions between electrolyte components. In conclusion, these experimental results show that TMPEI is a structurally stable additive material that does not undergo any additional chemical reactions. At the same time, TMPEI exhibits strong adsorption ability, ensuring the high reliability and stability of the SEI layer during prolonged cycling.

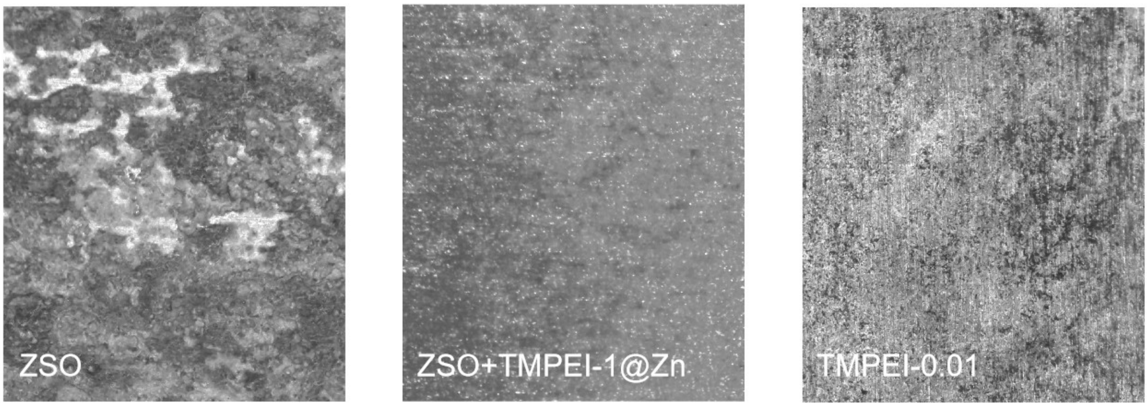

Fig. S16 OM observations of the zinc anodes after 80 min of electroplating at 1 mA cm^{-2}.

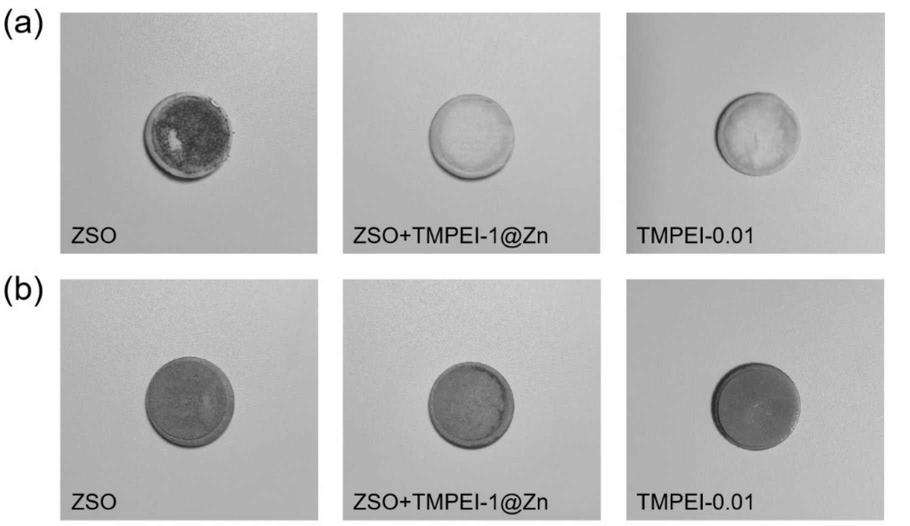

Fig. S17 (a) and (b) show the morphologies of the separators and zinc anodes after 100 h of galvanostatic cycling at 1 mA cm^{-2} and 1 mAh cm^{-2} for Zn||Zn symmetric cells.

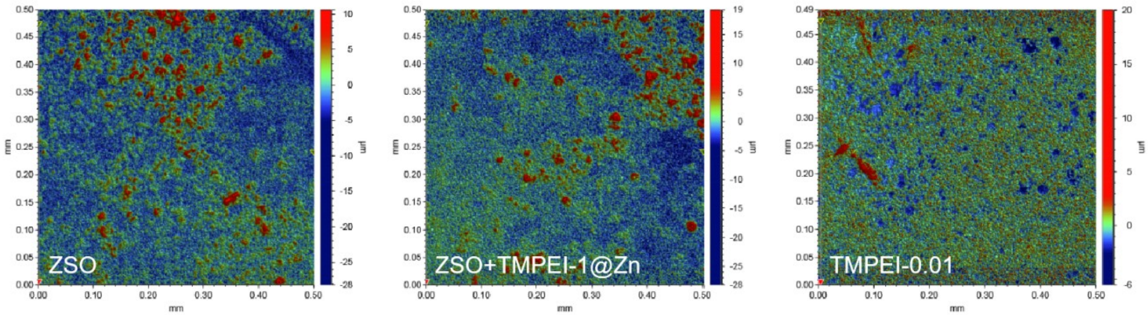

Fig. S18 Optical profilometer images of the surface roughness of zinc anodes after 100 h at 1 mA cm^{-2} and 1 mAh cm^{-2}.

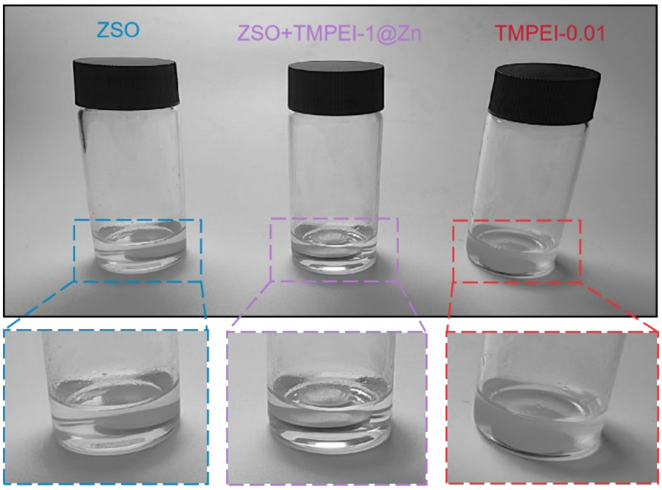

Fig. S19 Appearance of solutions after 8 days of soaking zinc foils in ZSO and TMPEI-0.01 electrolytes, and soaking of TMPEI-1@Zn electrode in ZSO electrolyte.

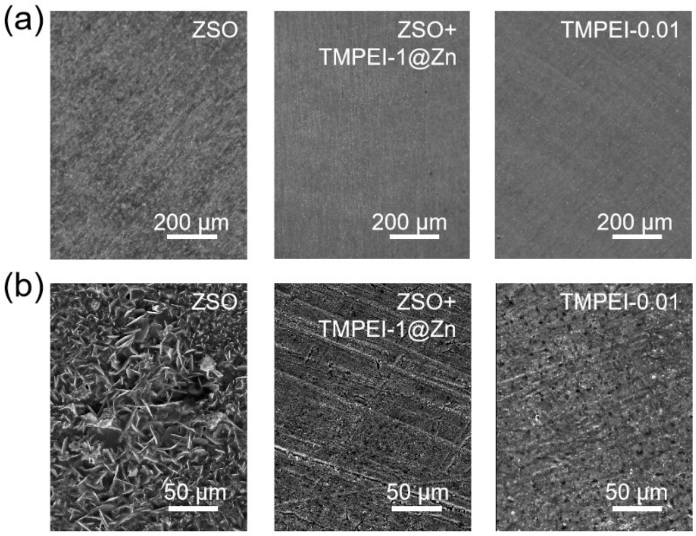

Fig. S20 (a) and (b) show the OM and SEM observations of zinc anodes after the three soaking experiments.

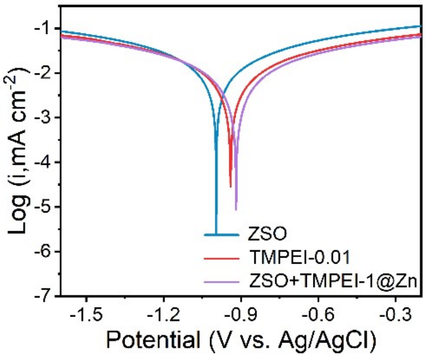

Fig. S21 Tafel curves of zinc anodes measured in three types of batteries.

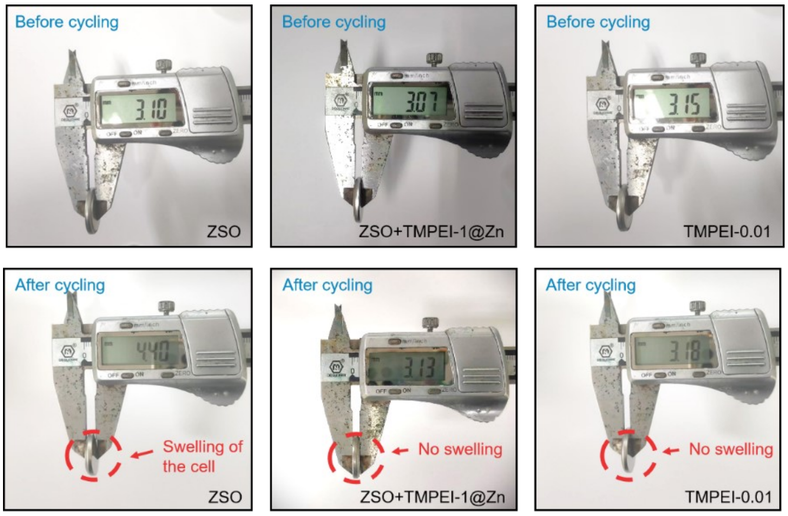

Fig. S22 Thickness changes of Zn||Zn symmetric cells before and after 100 h of galvanostatic cycling at 1 mA cm^{-2}and 1 mAh cm^{-2}.

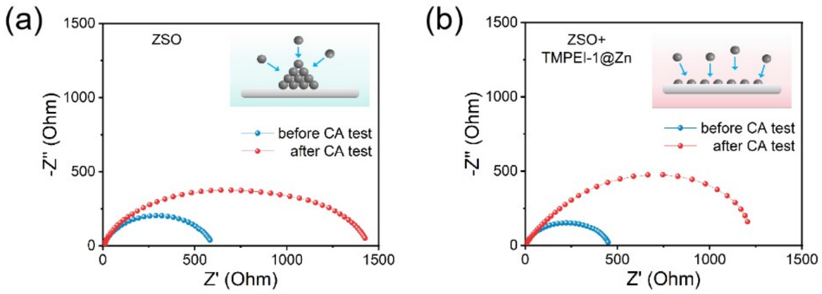

Fig. S23 (a) and (b) show the changes in Rct before and after CA testing for the ZSO and ZSO+TMPEI-1@Zn cells, respectively.

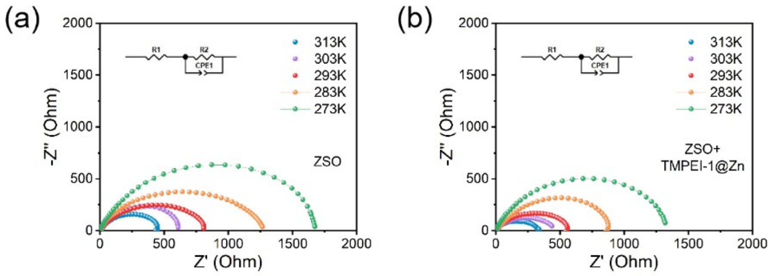

Fig. S24 (a) and (b) show the Nyquist EIS plots of the ZSO and ZSO+TMPEI-1@Zn cells, respectively, measured at different temperatures (273–313 K).

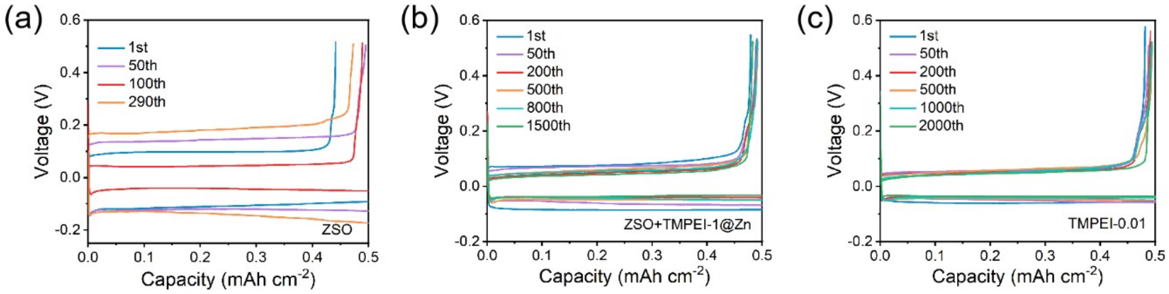

Fig. S25 Voltage-capacity curves of Zn||Cu half-cells with (a) ZSO electrolyte, (b) TMPEI-1@Zn electrode, and (c) TMPEI-0.01 electrolyte.

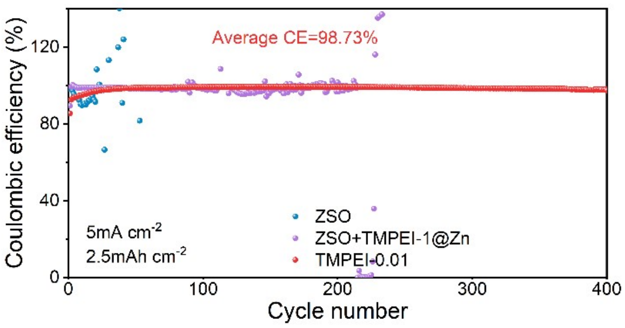

Fig. S26 Galvanostatic cycling performances of Zn||Cu half-cells at 5 mA cm^{-2} and 2.5 mAh

cm^{-2}.

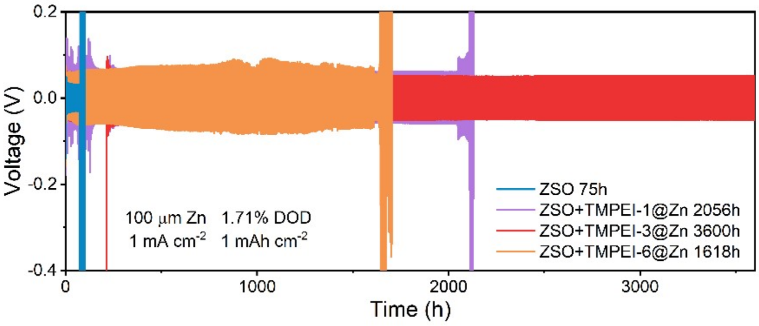

Fig. S27 Cycling performance of ZSO+TMPEI-n@Zn cells at 1 mA cm^{-2} and 1 mAh cm^{-2}.

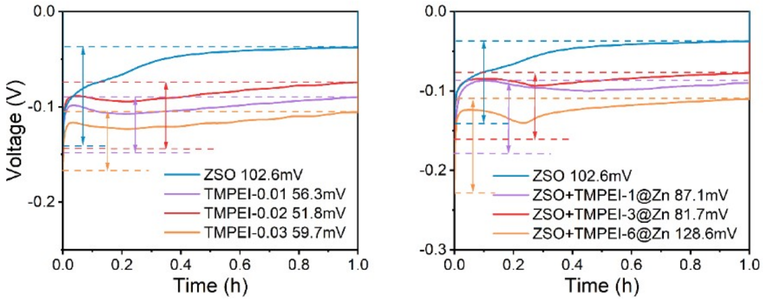

Fig. S28 Nucleation overpotential of Zn||Zn symmetric cells at 1 mA cm^{-2} and 1 mAh cm^{-2}.

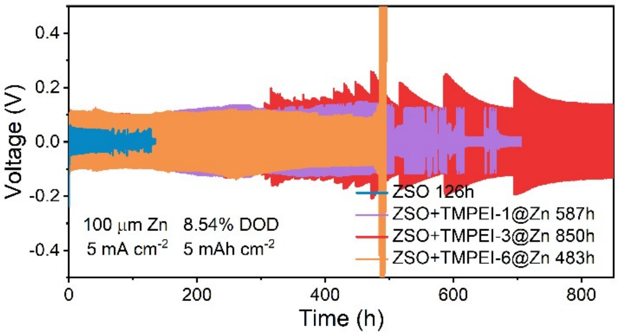

Fig. S29 Cycling performance of ZSO+TMPEI-n@Zn cells at 5 mA cm^{-2} and 5 mAh cm^{-2}.

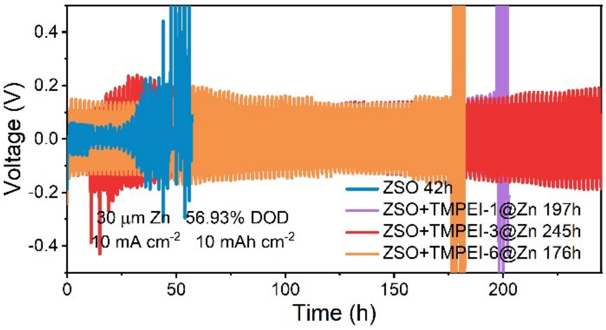

Fig. S30 Cycling performance of ZSO+TMPEI-n@Zn cells at 10 mA cm^{-2} and 10 mAh cm^{-2}.

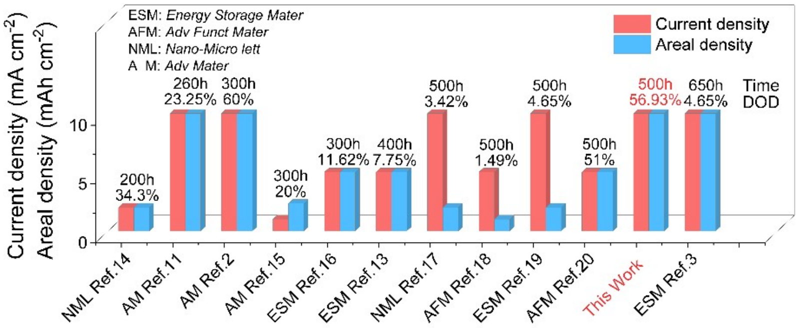

Fig. S31 Comparison of the working performance of Zn||Zn symmetric cells at 10 mA cm^{-2}.

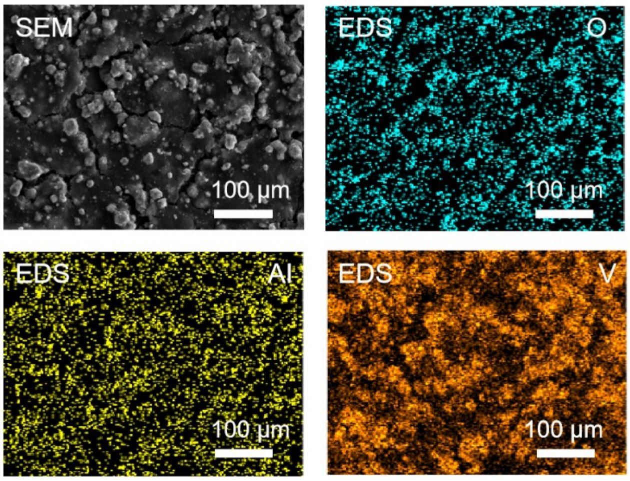

Fig. S32 SEM observations of the AlVO-NMP cathode and corresponding EDS mapping of the distribution of oxygen, aluminum, and vanadium elements.

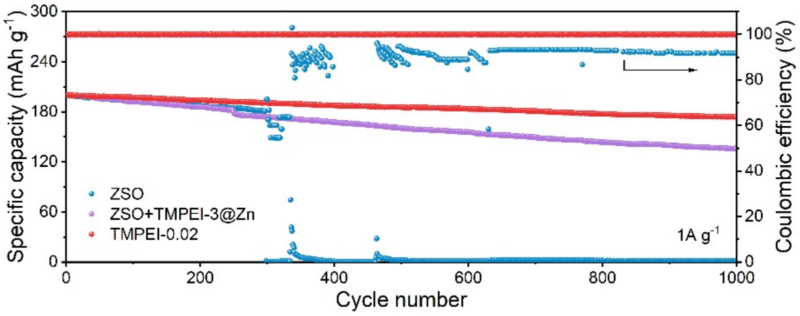

Fig. S33 Cycling performance of Zn||AlVO-NMP full cells at 1 A g^{-1}.

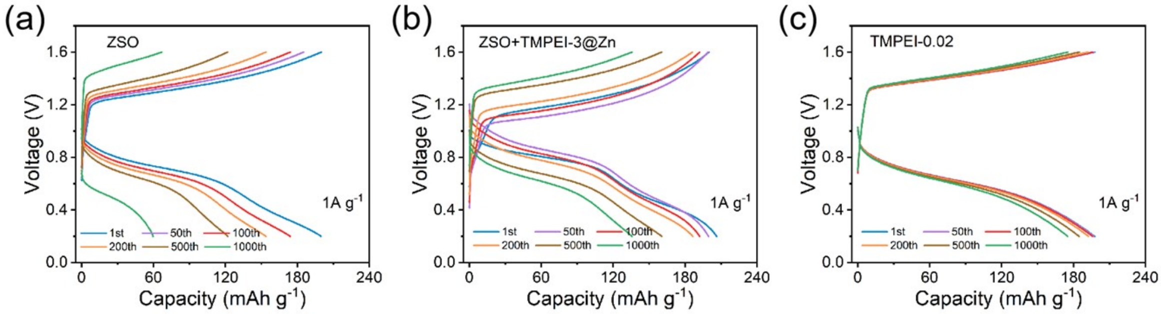

Fig. S34 (a), (b), and (c) show the GCD curves of the ZSO cell, ZSO+TMPEI-3@Zn cell, and TMPEI-0.02 cell, respectively.

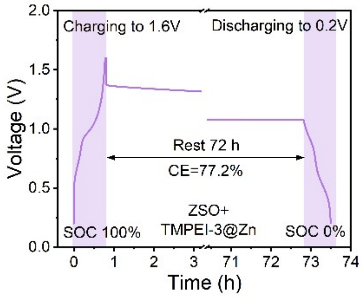

Fig. S35 Self-discharge performance of Zn||AlVO-NMP full cell using ZSO electrolyte and TMPEI-3@Zn electrode.

Table S1. Total surface energy of Zn foil and TMPEI-1@Zn calculated using the Owens-Wendt equation.

Electrode	γ_S	γ_S^d	γ_S^P
Zn foil	40.3	27.1	13.2
TMPEI-1@Zn	33.2	24.5	8.7

Table S2. Comparison of the cycling lifespan of reported AZIBs under constant current conditions.

Electrode	Electrolyte	Current density (mA cm^{-2})	Areal density (mAh cm^{-2})	Worked time (h)	DOD (%)	Ref.
Zn	2M Zn(OTF)$_2$ +30wt% DEG	5	5	600		[1]
Zn@ Bi/Bi$_2$O$_3$	2 M ZnSO$_4$	5	2.5	750	6.4	[2]
		10	10	300	60	
Zn	2M ZnSO$_4$+uridine	5	5	850		[3]
		10	1	650	4.65	
Zn	Zn(OTF)$_2$+β-CD	5	5	900		[4]
		10	1	500		
FAZ@Zn	2 M ZnSO$_4$	5	5	1000		[5]
Zn	3 M ZnSO$_4$ +0.5 g L^{-1} CS	5	5	1000		[6]

C-ZSL@Zn	2 M $ZnSO_4$	3	3	1100		[7]
		10	1	550		
HEO-CNFs	2 M $ZnSO_4$	5	2.5	1500		[8]
Zn	2 M $ZnSO_4$ +0.5 wt% PGA	2	1	1600		[9]
HR-BC -Zn	2 M $ZnSO_4$	5	1	1650		[10]
$(CS/SA)_4$ -Zn	2 M $ZnSO_4$	5	2.5	1750		[11]
		10	10	260	23.25	
HT-Zn	1 M $ZnSO_4$	1	0.5	1800		[12]
		10	5	90		
Zn	2 M $ZnSO_4$ +1M Z10	1	1	2000		[13]
		5	5	400	7.75	
ZnS	2 M $ZnSO_4$	3	1	1550		[14]
		2	2	200	34.3	
Zn	2 M $ZnSO_4$ + 0.5 mM C_8TAB	5	1	2500		[15]
		1	2.34	300	20	
Zn	2 M $ZnSO_4$+0.5wt%APG	5	5	300	11.62	[16]
Zn-SF	2 M $ZnSO_4$	10	2	500	3.42	[17]
Zn	2 M $ZnSO_4$ +0.1M NaDFOB	5	1	500	1.49	[18]
Zn	2M $ZnSO_4$ +0.01M NTA	10	2	500	4.65	[19]
Zn	2 M $ZnSO_4$ +0.2M SADS	5	5	500	51	[20]
TMPEI -3@Zn	**1M Zn(OTF)$_2$**	**5**	**5**	**850**	**8.54**	**This Work**
		10	**10**	**245**	**56.93**	
Zn	**1M Zn(OTF)$_2$+ 0.02wt% TMPEI**	**5**	**5**	**2000**	**8.54**	
		10	**10**	**500**	**56.93**	

Table S3. Comparison of the performance of TMPEI and other SEI protection strategies.

Electrode	Electrolyte	Current density (mA cm^{-2})	Areal density (mAh cm^{-2})	Worked time (h)	DOD (%)	CE (%)	Ref.
SnO_2/Zn|| SnO_2/Zn	2M $ZnSO_4$	0.5	0.5	3900	0.875		[21]
		4	8	800	14		
		10	10	200	35		

SnO$_2$/Zn||Cu		2	1	1000		99.30	
CDs/SnO$_2$@Zn|| SnO$_2$@Zn	2M ZnSO$_4$	2	0.5	2000	0.087		[22]
		5	1	500	0.174		
CDs/SnO$_2$@Zn|| Cu		2		800		99.6	
COF-PVDF@Zn|| COF-PVDF@Zn	2M ZnSO$_4$	1	1	>600	1.708		[23]
		1	3	>300	5.124		
		1	5	>280	8.54		
COF-PVDF@Zn|| Cu		1	1	140		>99	
TpPa-SO$_3$ H@Zn-foil|| TpPa-SO$_3$ H@Zn-foil	1M ZnSO$_4$	5	5	1000	8.54		[24]
TpPa-SO$_3$ H@Zn-foil||Cu		1	1	1000		99	
CMC-coted Zin foil|| CMC-coted Zin foil	1.5M ZnSO$_4$	1	0.1	200	0.171		[25]
		1	1	200	1.71		
CMC-coted Zin foil||Cu		1	1	100		99	
CB@Zn|| CB@Zn	2M ZnSO$_4$	0.5	0.5	1500	0.854		[26]
CB@Zn||Cu		2		500		99	
TMPEI -3@Zn|| **TMPEI -3@Zn**	**1M Zn(OTF)$_2$**	**1**	**1**	**3600**	**1.71**		**This Work**
		5	**5**	**850**	**8.54**		
		10	**10**	**245**	**56.93**		
TMPEI -3@Zn||Cu		**1**	**0.5**	**800**		**98.83**	
Zn||Zn	**1M Zn(OTF)$_2$+ 0.02wt% TMPEI**	**1**	**1**	**>4200**	**1.71**		
		5	**5**	**2000**	**8.54**		
		10	**10**	**500**	**56.93**		
Zn||Cu		**1**	**0.5**	**1050**		**99.27**	

To better highlight the advantages of the TMPEI SEI layer in terms of performance and practical feasibility, we compared TMPEI with other common SEI methods (Table S3). Firstly, common SEI methods such as metal oxides[21,22], COFs[23], MOFs[24], poly-electrolytes[25], and anchored layered structures[26] provide certain levels of zinc anode protection. However, these methods generally involve complex preparation processes. These SEI methods often require complex precursor synthesis, multi-step reactions, and strict environmental control, making the fabrication process cumbersome. In contrast, whether by using TMPEI as an additive to construct an in situ SEI layer or by soaking to construct an artificial SEI layer, the TMPEI method demonstrates significant advantages in simplifying the preparation process, offering greater practical feasibility.

Secondly, from the analysis of Table S3, it is evident that compared to other strategies, the SEI layer constructed using TMPEI enables symmetric batteries to exhibit longer cycle life and higher DOD under low current (1 mA cm^{-2}), high current (5 mA cm^{-2}), and ultra-high current (10 mA cm^{-2}) conditions, fully demonstrating TMPEI's outstanding performance in enhancing battery performance. Meanwhile, the SEI layer constructed by TMPEI allows the Zn||Cu half-cell to achieve stable cycling for up to 1050 h at 1 mA cm^{-2}, with a Coulombic efficiency of 99.27%. Compared to other strategies, this performance also shows significant advantages, further highlighting TMPEI's excellent performance in improving battery efficiency.

In addition, compared to other strategies, the use of TMPEI helps to construct a more stable and durable SEI layer. The SEI strategies mentioned above have an inherent issue: they are typically composed of components that are difficult to self-repair, and once ruptured, they are hard to recover. However, the high stability of the TMPEI structure allows it to maintain structural integrity during prolonged cycling. At the same time, the high zinc affinity of the terminal thiol groups gives TMPEI strong adsorption capability on the zinc anode surface. Therefore, any unexpectedly detached TMPEI molecules have the opportunity to re-adsorb onto the zinc anode, imparting enhanced dynamic self-healing ability to the TMPEI-constructed SEI layer. This contributes to prolonging the cycling life of the battery and maintaining a higher battery capacity.

References

1 Z. Zhao, C. Tang, Y. Zhang, H. Zhang, X. Shi, H. Zhao, G. Wang, J. Liu and L. Li, *Energy Storage Mater.*, 2024, **70**, 103515.

2 X. Tian, Q. Zhao, M. Zhou, X. Huang, Y. Sun, X. Duan, L. Zhang, H. Li, D. Su, B. Jia and T. Ma, *Adv mater.*, 2024, **36**, e2400237.

3 J. Wu, B. Song, Z. Ge, X. Xiao, W. Deng, G. Zou, H. Hou and X. Ji, *Energy Storage*

Mater., 2023, **63**, 103000.

4 G. Zhang, L. Fu, Y. Chen, K. Fan, C. Zhang, H. Dai, L. Guan, M. Mao, J. Ma and C. Wang, *Adv Mater.*, 2024, **36**, 2405949.

5 T. Shen, M. Fang, L. Lv, H. Wu, O. Sheng, T. Yang, C. Dong, H. Ji, E. Zhang and X. Zhang, *Adv Funct Mater.*, 2024, **34**, 2408578.

6 J. Yang, M. Qiu, M. Zhu, C. Weng, Y. Li, P. Sun, W. Mai, M. Xu, L. Pan and L. Li, *Energy Storage Mater.*, 2024, **67**, 103287.

7 J. H. Park, C. Choi, J. B. Park, S. Yu and D. W. Kim, Adv. *Energy Mater.*, 2024, **14**, 2302493.

8 Y. Li, H. Jia, U. Ali, H. Wang, B. Liu, L. Li, L. Zhang and C. Wang, Adv. *Energy Mater.*, 2023, **13**, 2301643.

9 C. Huang, J. Mao, S. Li, W. Zhang, X. Wang, Z. Shen, S. Zhang, J. Guo, Y. Xu and Y. Lu, *Adv. Funct. Mater.*, 2024, **34**, 2315855.

10 K. Liu, Y. Li, T. Zhang, A. Zhu, G. Gan, D. Lin, K. Liu, C. Luan, S. Bu and X. Zhang, *Adv. Funct. Mater.*, 2024, **34**, 2409251.

11 X. Cai, X. Wang, Z. Bie, Z. Jiao, Y. Li, W. Yan, H. J. Fan and W. Song, *Adv. Mater.*, 2024, **36**, 2306734.

12 B. Ren, S. Hu, A. Chen, X. Zhang, H. Wei, J. Jiang, G. Chen, C. Zhi, H. Li and Z. Liu, *Adv. Energy Mater.*, 2024, **14**, 2302970.

13 L. Tao, K. Guan, R. Yang, Z. Guo, L. Wang, L. Xu, H. Wan, J. Zhang, H. Wang and L. Hu, *Energy Storage Mater.*, 2023, **63**, 102981.

14 Y. Chen, Z. Deng, Y. Sun, Y. Li, H. Zhang, G. Li, H. Zeng and X. Wang, *Nano-Micro Lett.*, 2024, **16**, 96.

15 D. Tang, X. Zhang, D. Han, C. Cui, Z. Han, L. Wang, Z. Li, B. Zhang, Y. Liu and Z. Weng, *Adv. Mater.*, 2024, **36**, 2406071.

16 H. Wang, M. Zhu, H. Wang, C. Li, Z. Ren, Y. Zhang, S. Chen, H. Li, D. Chen and Z. Bai, *Energy Storage Mater.*, 2024, **67**, 103238.

17 M. Zhu, Q. Ran, H. Huang, Y. Xie, M. Zhong, G. Lu, F. Bai, X. Lang, X. Jia and D. Chao, *Nano-Micro Lett.*, 2022, **14**, 219.

18 Z. Wang, J. Diao, G. Henkelman and C. B. Mullins, *Adv. Funct. Mater.*, 2024, **34**, 2314002.

19 Z. Liang, C. Li, D. Zuo, L. Zeng, T. Ling, J. Han and J. Wan, *Energy Storage Mater.*, 2023, **63**, 102980.

20 Y. Ding, L. Yin, T. Du, Y. Wang, Z. He, J. A. Yuwono, G. Li, J. Liu, S. Zhang and T.

Yang, *Adv. Funct. Mater.*, 2024, **34**, 2314388.

21 Y. Zhang, P. Chen, M. Li, S. Li, Y. Yue, Y. Wang, S. Xie and W. Zhou, *J. Mater. Chem. A*, 2023, **26**, 14333-14344.

22 M. Gopalakrishnan, M.T. Hlaing, T. Kulandaivel, W. Kao-ian, M. Etesami, W.-R. Liu, M.T. Nguyen, T. Yonezawa, W. Limphirat and S. Kheawhom, *J. Alloys Compd*, 2025, **1013**, 178521.

23 V. Aupama, J. Sangsawang, W. Kao-ian, S. Wannapaiboon, J. Pimoei, W. Yoopensuk, M. Opchoei, Z. Tehrani, S. Margadonna and S. Kheawhom, *Electrochim. Acta*, 2024, **506**, 145059.

24 J. Zhao, Y. Ying, G. Wang, K. Hu, Y.D. Yuan, H. Ye, Z. Liu, J.Y. Lee and D. Zhao, *Energy Storage Mater.*, 2022, **48**, 82-89.

25 P. Tangthuam, W. Kao-ian, J. Sangsawang, C. Rojviriya, P. Chirawatkul, J. Kasemchainan, F. Mahlendorf, M.T. Nguyen, T. Yonezawa and S. Kheawhom, *Mater. Sci. Energy Technol.*, 2023, **6**, 417-428.

26 Z. Peng, H. Yan, Q. Zhang, S. Liu, S.C. Jun, S. Poznyak, N. Guo, Y. Li, H. Tian, L. Dai, L. Wang and Z. He, *Nano Lett*, 2024, **24**, 9137-9146.